PUBLICATION

MUSTANG

A MUltiple Space and Time scale Approach for the quaNtification of deep saline formations for CO_2 storaGe

Project Number:227286

AUTHORS: Zhibing Yang [1]*, Liang Tian 1, Auli Niemi 1, Fritjof Fagerlund [1]

[1]Department of Earth Sciences, Uppsala University, Villavägen 16, 75236 Uppsala, Sweden

*Corresponding author (zhibing.yang@hyd.uu.se)

TITLE: Upscaling of the constitutive relationships for CO2 migration in multimodal heterogeneous formations

The research leading to these results has received funding from the European Community's Seventh Framework Programme [FP7/2007/2013) under grant agreement n° [227286]

Status	AUTHOR VERSION
Date	Accepted: 11 December 2012
Publisher	International Journal of Greenhouse Gas Control
Reference	DOI 10.1016/j.ijggc.2012.11.015



Submitted for publication to International Journal of Greenhouse Gas Control, 2012

Upscaling of the constitutive relationships for CO_2 migration in multimodal heterogeneous formations

Zhibing Yang [1*], Liang Tian [1], Auli Niemi [1], Fritjof Fagerlund [1]

[1]Department of Earth Sciences, Uppsala University, Villavägen 16, 75236 Uppsala, Sweden

*Corresponding author (zhibing.yang@hyd.uu.se)

Abstract.

Numerical modeling is a critical tool for site performance and risk assessment of geological stored CO_2 at the reservoir scale. However, due to computational resource constraints, reservoir scale models have limitations in accounting for the details of the multi-scale heterogeneities. Appropriately averaged medium parameters are needed for the full scale modeling. In this study, we apply the macroscopic theory and present large-scale capillary pressure-relative permeability-saturation relationships that may be used as grid-block properties in the full-scale modeling. A macroscopic invasion percolation (MIP) model is developed, based on the assumption of capillary force dominance. Comparison of the MIP model with the numerical simulator TOUGH2/ECO2N for simulations of large-scale drainage capillary pressure curves shows a reasonably good match between results from the two models. Large-scale constitutive relationships are obtained through simulation procedures of CO_2 displacing brine in multimodal heterogeneous media for ten cases with different geostatistical parameters. The large-scale constitutive relationships are mainly controlled by the proportion and the permeability variability of the background (framework) material, while the existence of the non-framework materials and their

permeability variabilities may contribute, in a complex way, to the uncertainty in the large-scale constitutive relationships. In addition, the Leverett equation may well describe the relationship between the large-scale capillary pressure and absolute permeability when the sandstone (background material) proportion is high (>0.7). For cases with smaller sandstone proportions it may not be appropriate to link capillary pressure and absolute permeability through the Leverett equation.

Keywords: constitutive relationship; two-phase flow; CO2 storage; macroscopic percolation; Leverett scaling; numerical modeling.

Introduction

Evaluating the performance of CO_2 geological storage requires a thorough understanding of the physical processes that determine the long term fate of the injected CO_2. Being able to model the physical processes at the relevant scales for the sequestration is central for this. Geologic formations are heterogeneous at various length scales (Tsang et al., 2007; Ambrose et al., 2008; Ringrose et al., 2008). Due to the geological heterogeneity the effective parameters for the large-scale behavior can be significantly different from those for the small-scale behavior. As a matter of fact, it may be difficult even to define representative effective parameters and relationships for many processes, if both the geological heterogeneity and the actual processes are complex. However, it is more than often computationally prohibitive to simulate CO_2 storage in a heterogeneous formation with a detailed resolution of the spatial variability. Therefore approaches for upscaling and defining large-scale effective parameters and relationships need to be explored.

Spatial variability also leads to uncertainty as the sampled part of the porous media often accounts for only a very small fraction of the formation under investigation. Upscaling techniques (and/or effective parameters and constitutive relations) as well

as uncertainty quantification are thus practically needed, while complexities and challenges are imposed by the multi-scale heterogeneity in combination with the highly nonlinear multiphase flow system. In this study, we consider three scales: (i) core scale (0.1~1 m); (ii) lithofacies scale (1 ~ 10m) and (iii) block scale (several tens of meters, as considered to be the size of a grid-block in a reservoir model). We perform two-phase numerical simulations at the block scale and observe the effective behavior of permeability as well as the two-phase characteristics functions, namely the capillary pressure–saturation relationship and the relative permeability–saturation relationship. In the block-scale model we include the detailed heterogeneity and vary the statistical characteristics of this variability. Simulations are carried out in a multiple-realization Monte Carlo mode.

As the computational effort would become extremely intensive by use of full two-phase flow simulations, we are introducing and using an alternative approach named macroscopic invasion percolation (MIP) method. This method will first be shortly introduced and the results compared to those from full multiphase flow simulations.

The overall objective of the work is to see how the characteristics of geological heterogeneity influence the upscaling behavior of the characteristic functions for two-phase flow.

Background

Geological storage of CO_2 by injection into the deep saline formations can be characterized by a two-phase system where the injected supercritical CO_2 (non-wetting phase) displaces the resident formation water. Numerical models are critical for the understanding of such system (e.g. Pruess and Garcia, 2002; Juanes et al., 2006; Doughty, 2007).

As in the case of other two-phase processes such as unsaturated flow in the vadose zone and oil production in petroleum reservoirs, geologic heterogeneity imposes challenges for predictive modeling of the CO_2 migration at the large scale. In order to quantify the impact of heterogeneity, there have been considerable recent efforts to understand the CO_2 migration behavior in heterogeneous geological formations (e.g., Doughty and Pruess, 2004; Obi and Blunt, 2006; Flett et al., 2007; Lengler et al., 2010; Saadatpoor et al., 2010; Han et al., 2010; Shamshiri and Jafarpour, 2012). Doughty and Pruess (2004) created three-dimensional Markov-chain models, representing the fluvial/deltaic Frio Formations in the Umbrella Point power plant site and South Liberty pilot test site, to estimate subsurface CO_2 migration and storage capacity. Flett et al. (2007) investigated the effects of binary geologic systems (with various proportions of sand and shale) on residual CO_2 trapping and suggested that an increase in shale content increases tortuosity in CO_2 migration pathways and, consequently, reduces the rate of residual CO_2 trapping. In the full-scale three-dimensional model of Doughty and Pruess (2004), Obi and Blunt (2006) and Flett et al. (2007), a more detailed description of the small-scale permeability distribution may have been neglected because of the limited grid resolution (Lengler et al., 2010).

Formation heterogeneity is dependent on the depositional environment and manifests itself both in the geometry and spatial distribution of the depositional facies as well as the spatial permeability distribution within the facies (Lengler et al., 2010). This indicates that the permeability distribution of a storage formation may be best represented by a multimodal distribution with the number of modes corresponding to the number of hydrofacies (materials).

Technological constraints often limit the measurement of material properties (i.e., porosity, permeability, capillary pressure and relative permeability functions) to

sample supports (i.e., sample volumes) much smaller than can be accommodated in current predictive models (Tidwell and Wilson, 2000). This disparity in support scales together with the spatial variability in the properties requires measured data be averaged or upscaled to yield effective properties at the desired scale of analysis.

A number of methods have been aimed at providing large-scale average properties for two-phase systems in heterogeneous media. Stochastic analyses by e.g. Yeh et al. (1985a, b), Mantoglou and Gelhar (1987) and Zhang (1999) have shown that large-scale effective parameters for two-phase flow depend in a complex way on the stochastic parameters representing local properties. Quintard and Whitaker (1990) have developed a volume-averaging method to evaluate the large-scale capillary pressure and relative permeability curves. Upscaled models for unsaturated flow have also been developed using homogenization theory (e.g., Lewandowska et al., 2004; Neuweiler and Vogel, 2007). Mouche et al. (2010) presented an upscaled model for the vertical migration of a CO_2 plume through periodic layered porous media adopting the homogenization procedures. Gasda and Celia (2005) showed that upscaling of relative permeability by analytical pseudo-functions (i.e., effective relative permeability is simply a permeability-weighted average of local relative permeability) cannot capture the two-phase flow dynamics even for a simple heterogeneous problem of a single high permeability streak in a low-permeability background medium. Recently, Bolster et al. (2009) and Bolster et al. (2011) have derived large-scale effective flow equation for the saturation of the displacing fluid for the Buckley-Leverett problem, in an effort to quantify the impact of heterogeneity on the spreading and dispersion of the saturation front, which enhances the surface area between the fluids and thus the dissolution trapping efficiency of CO_2. Recently, Silva et al. (2012) presented an effective model of 1D saturation equation with mass

exchange between the mobile and immobile zones which accounts for the local-scale non-equilibrium due to the medium heterogeneity.

The application of percolation theory to the large-scale averaging of capillary pressure and relative permeability for two-phase/unsaturated flow has also been reported in the literature (Kueper and McWhorter, 1992; Ewing and Gupta, 1993; Yortsos et al., 1993; Ioannidis et al., 1996; Braun et al., 2005). Note that we will use large-scale interchangeably with block-scale as defined in the introduction to follow the convention from these earlier works. Kueper and McWhorter (1992) were the first to introduce the macroscopic percolation approach. This approach is analogous to the classical microscopic percolation theory (Wilkinson and Willemsen, 1983) in that the structure of the porous medium is represented as an ordered lattice, but differs in that each point of the lattice is assigned a local-scale porosity, permeability and capillary pressure-saturation relationship, rather than microscale pore and pore throat dimensions. Application of the percolation theory requires an infinitesimal flow rate where the capillary forces dominate over the viscous forces. Such flow conditions can be approached as the capillary number $N_{ca} = \mu v/\sigma$ tends to zero, where μ is the viscosity of the supercritical CO_2, v is the Darcy velocity and σ is the interfacial tension. According to Lenormand et al. (1988), N_{ca} should be smaller than about 10^{-7} to qualify capillary dominant conditions, for the viscosity ratio about 0.1 of the CO_2-brine system. In a typical radial CO_2 injection scenario, the condition (small flow rate) generally can be met except in the region of immediate vicinity of the injection well, given that the velocity damps down quickly with increasing radial distance. For example, given $v = 10^{-6}$ m/s, $\mu = 5.25\times10^{-5}$ Pa·s (Juanes et al., 2006) and $\sigma = 0.036$ N/m (Pini et al., 2012), N_{ca} is 1.5×10^{-9}, while a velocity of 10^{-6} m/s at a radial distance of 100 m in a 50 m thick layer corresponds to an injection rate of 0.75 Mt CO_2 per year, which is on the scale of a commercial project (IPCC, 2005).

Ioannidis et al. (1996) concluded that the large-scale capillary pressure and relative permeability behavior of a heterogeneous system is strongly dependent on the structure of the permeability field and can be explained in terms of macroscopic accessibility and trapping. Although percolation concepts are generally considered as a physically sound approach for the problem of quasi-static, immiscible displacement at the pore scale, large-scale capillary pressure curves obtained through application of macroscopic percolation theory have not been compared with those obtained through experimental measurements or numerical solutions to the two-phase problem. Furthermore, the aforementioned applications of the percolation theory have mainly relied on single or a few realizations for different permeability field structures, uncertainty in the large-scale constitutive relations has not been discussed.

Although a few studies have been conducted on flow and solute transport in a multimodal heterogeneous medium (Desbarats, 1990; Rubin, 1995; Russo et al., 2001; Lu and Zhang, 2002), no investigation has been reported on large-scale two-phase constitutive relationships in multimodal heterogeneous formations, which is the topic of this study. Specifically, we apply the macroscopic percolation theory to CO_2 migration in trimodal heterogeneous media with sandstone (background material), siltstone and clay, and then study the effect of material proportions and spatial distribution of the local-scale attributes within each material.

Methods

In the following, we will first present the macroscopic invasion percolation (MIP) model. We then proceed to the assignment of local properties and the generation of multimodal heterogeneous media using transition-probability based geostatistics.

The model

It is assumed that the large-scale displacement of brine by supercritical CO_2 can be represented by a macroscopic percolation process in a heterogeneous formation with a lattice representation of a macroscopic continuum. Here, we focus on the primary drainage process which occurs during the CO_2 injection period. Unlike the microscopic percolation where each node or cell is occupied by only one fluid, the macroscopic percolation theory adopted here allows for bicontinua of fluids in each node (Kueper and McWhorter, 1992). Each node (cell) is given a local permeability, capillary pressure-saturation function and relative permeability-saturation function.

Percolation theory is strictly applicable only in the limit of the dominance of capillary forces over viscous forces. In addition, gravity (buoyancy) force may play a role during the displacement process. In order to fulfill the requirement that the viscous forces and gravity forces be small, relative to capillary forces at the length scale of a cell, the cell size l cannot be assigned arbitrarily (Ioannidis et al., 1996). Both viscous forces and gravity forces increases with cell size. The cell size over which viscous forces will become comparable to capillary forces may be estimated as $l \sim kP_{cd}/\mu v$, where k is the local permeability and P_{cd} is a characteristic capillary pressure (e.g., the entry pressure in the Brooks-Corey function). For example, given a CO_2-brine system with an average velocity of 10^{-6} m/s, a permeability of 2.76×10^{-13} m^2, a CO_2 viscosity of 5.25×10^{-5} Pa·s and a characteristic capillary pressure of 3192 Pa, the above estimation gives a length scale of about 17 m, which is much larger than the cell size 0.5 m in the displacing direction as used in this work, indicating that viscous force may be negligible. The error in large-scale capillary pressure relationships resulting from the application of the percolation model which ignores viscous forces, as compared with those obtained with the numerical simulator TOUGH2/ECO2N (Pruess et al., 1999; Pruess and Spycher, 2007), will be discussed in Section 4.1. In

this study, it is also assumed that the buoyancy effect on the large-scale capillary pressure relations is small, given that the thickness of the heterogeneous medium is relatively small (a few meters) and that the heterogeneity due to the existence of siltstone layers and clay lenses strongly mitigates the rising of CO_2 through the formation (Flett et al., 2005).

Primary drainage commences with all nodes first being fully saturated by the formation brine (wetting phase). The non-wetting phase (supercritical CO_2) is then allowed to invade the network from any given boundary at a specified, externally applied pressure difference ΔP_{ex}. The non-wetting fluid may invade a given available cell (neighboring to the invaded cells) at this external pressure difference, provided that the following two conditions are satisfied: (1) the local displacement (entry) pressure is exceeded ($\Delta P_{ex} \geq P_{cd}$); (2) the wetting fluid in the cell is not macroscopically trapped. Following the work of Ioannidis et al. (1996), we define macroscopically trapped cells (which have virtually immobile wetting phase) as the cells that have capillary pressure $P_c \geq 10P_{cd}$ or are surrounded by cells with capillary pressure $P_c \geq 10P_{cd}$, corresponding to values of wetting phase saturation S_w only slightly lower than residual wetting phase saturation S_{wr}. However, unlike the model of Ioannidis et al. (1996), we only allow some of the available cells satisfying the two conditions to be invaded at each percolation step. For a heterogeneous field, it is expected that at each step the invasion driving forces for different available cells (which may be estimated as $\Delta P_{ex} - P_{cd}$) may vary significantly in space. Hence, the time scales for completing the invasion of these cells may also vary significantly, suggesting the possibility of trapping of the cells with small invasion forces by those with vary large invasion forces. To represent this trapping possibility in the model, we introduce a simple parameter τ ($0 \leq \tau \leq 1$) which essentially divides the available cells into two groups (one with smaller invasion forces and the other with larger invasion

forces). At each step only the available cells belonging to the latter group are invaded. This is done by adding a third invasion condition (which is stricter than the aforementioned first condition if $\tau < 1$) as follows:

$$\Delta P_{ex} \geq (1-\tau)\cdot \max(\Delta P_{ex} - P_{cd}) + P_{cd} \qquad (1)$$

When $\tau = 1$, equation (1) reduces to the first condition and the model is then similar to that of Ioannidis et al. (1996); when $\tau = 0$, only the cell with maximum driving force (or minimum capillary resistance) is invaded and the model is similar to the classical invasion percolation model (Wilkinson and Willemsen, 1983). In section 4.1, we will test the parameterization for τ with the aid of numerical two-phase flow simulations.

Once a cell has been invaded, supercritical CO_2 may continue to advance to a neighboring cell if the aforementioned three conditions are satisfied. After a sweep of the lattice for a given ΔP_{ex}, the local saturation values for the invaded cells are calculated according to the local capillary pressure functions (described in Sectioin 3.2), and then the large-scale average capillary pressure is calculated as (Kueper and McWhorter, 1992):

$$P_{c,L} = \frac{1}{V_{NW}} \int_{V_{NW}} P_{NW}\, dV_{NW} - \frac{1}{V_W} \int_{V_W} P_W\, dV_W \qquad (2)$$

where $P_{c,L}$ is the large-scale average capillary pressure, P_{NW} and V_{NW} are the local non-wetting phase (CO_2) pressure and the total volume of the non-wetting fluid, and P_W and V_W are the local wetting phase pressure and the total volume of the wetting fluid. The average non-wetting phase saturation is $S_{nw,L}$ given by

$$S_{nw,L} = \frac{\int V_{NW}\, dV}{V \int \phi dV} \qquad (3)$$

where V is total volume of the system and ϕ is the local porosity; the average wetting phase saturation $S_{w,L}$ is given by

$$S_{w,L} = \frac{\int V_w \, dV}{V \int \phi dV} \qquad (4)$$

To construct the large-scale capillary pressure curve, the simulation proceeds with incrementally increasing of ΔP_{ex}. Each small increment produces a fluid distribution which gives a ($S_{w,L}$, $P_{c,L}$) point on the curve. The fluid distribution associated with each $P_{c,L}$ also contains the local saturation information which can be used to calculate the local relative permeabilities k_{rw} and k_{rn}. Large-scale average relative permeabilities can be computed through the application of a single-phase flow-averaging method (Eichel et al., 2005), as follows. It is assumed that the motion of one fluid has no impact on that of the other fluid. Imposing a unit pressure gradient, we solve the pressure equation for a single phase. We then determine the velocity field from the pressure distribution of the single fluid. Subsequently, the effective permeability of the phase considered, k_{eff} (associated with a large scale average saturation S), is calculated from the mean velocity and the applied pressure gradient. The relative permeability is calculated as the ratio between k_{eff} (S) and k_{eff} (S = 1). Repeating this procedure for different $P_{c,L}$ and thus different S, we obtain the relative permeability curves for the principle displacement direction. It should pointed out that relative permeabilities resulting from upscaling should generally be expected to be a tensorial rather than a scalar function of saturation (Eichel et al., 2005; Keilegavlen et al., 2012; Wolff et al., 2012). However, proper handling of tensorial relative permeabilities in numerical models is under development (see recent studies of e.g., Keilegavlen et al., 2012; Wolff et al., 2012) and not fully tackled. To simplify the analysis, we present the upscaled relative permeabilities only as one of diagonal entries in the tensors for both phases in the principle direction of displacement (horizontal). The focus is to investigate how heterogeneity structure affects the relative permeabilities in this direction.

Local properties

We consider a two-dimensional heterogeneous section (40 m × 5 m) that is composed of a rectangular array of cells with four connections per cell. The array is assigned a local permeability value to each cell, assuming that the permeability follows a multimodal distribution. Based on the well log data from deep borehole FFC-1 at Southwest Scania site in Sweden, a site suitable for geological sequestration, the heterogeneous medium is characterized by three lithofacies (materials), namely sandstone, siltstone and clay (Gunnarsson, 2011) with the sandstone denoted as the background facies. The sandstone may be further differentiated by grain size into fine-grained and medium-grained sandstones. However, in this study, we do not differentiate them as we adopt a multimodal distribution and different grain sizes are represented by heterogeneities within the material. We follow the methodology as detailed in Lu and Zhang (2002) to generate the multimodal heterogeneous media. We first generate 100 two-dimensional (80 × 50) Markovian random fields of the three materials with specified material proportions and mean lens lengths in both directions, using Transitional Probability Geostatistical Software (T-ProGS) developed by Carle and Fogg (1996, 1997). We then generate, for each material, 100 realizations of two dimensional (80 × 50) Gaussian fields with zero mean, unit variance and specified correlation lengths (assuming a log-normal distribution and a spatial correlation structure represented by an exponential variogram), using a random field generator HYDRO_GEN (Bellin and Rubin, 1996). Multimodal heterogeneous realizations are then obtained through combining each Markovian random field with three Gaussian realizations (for the three materials) that are scaled from zero mean and unit variance to the specified means and variances. This results in a total of 100 realizations. An example realization is shown in Fig. 1a.

Once the multimodal heterogeneous permeability field has been generated, local-scale capillary pressure-saturation curves are assigned to each cell assuming that the local capillary pressures are correlated to permeability according to Leverett scaling (Leverett, 1941):

$$P_c = c\sigma(k/\phi)^{-1/2} \quad (5)$$

where P_c is the local capillary pressure of interest, σ is the interfacial tension and c is an empirical constant.

We use a Brooks-Corey relationship (Brooks and Corey, 1964) to represent the local capillary pressure curves. The Brooks-Corey relationship is given by

$$S_e = (P_c / P_{cd})^{-\gamma} \quad (6)$$

where γ is the local-scale pore size distribution parameter and S_e is an effective wetting phase saturation given by

$$S_e = (S_W - S_{wr})/(1 - S_{wr}) \quad (7)$$

where S_{wr} the local residual wetting phase saturation. The local description of wetting phase and non-wetting phase relative permeabilities is given as (Brooks and Corey, 1964):

$$k_{rw} = (S_e)^{3+2/\gamma} \quad (8)$$

$$k_{rn} = (1 - S_e)^2 \left[1 - (S_e)^{1+2/\gamma}\right] \quad (9)$$

Simulation outline

A series of simulations have been carried out to investigate the effect of multimodal heterogeneities (as characterized by material proportions, standard deviations and correlation lengths within the category) on large-scale capillary pressure and relative permeability relations. In total 10 cases are considered. We simulate the brine displacement by CO_2 in the horizontal direction with specified ΔP_{ex}, while keeping the

top and bottom as impermeable boundaries. For each case 100 realizations have been simulated. Table 1 lists the statistical parameters used for generating the permeability fields for all cases. These parameters correspond to a range of possible facies structures from analysis of the well-log data of Southwest Scannia site. Table 2 lists the corresponding local-scale parameters used in the simulations. The sandstone parameters are based on recent literature values presented by Pini et al. (2012) for a Berea sandstone sample. The siltstone parameters are assigned by assuming that the permeability is smaller than that of the sandstone by about one and half orders of magnitude (Kitajima et al., 2005). The clay permeability is set to be very low ($10^{-17}m^2$) such that the high entry pressure prevents CO_2 invasion into the clay material. The porosity is assumed to be uniformly 0.2 for simplicity.

Results

Comparison to TOUGH2/ECO2N simulations

In order to examine the performance of the macroscopic percolation theory for constructing the large-scale capillary pressure-saturation relationships, we first simulated, for comparisons purposes, eight realizations of Case 2 using the extensively applied multiphase flow simulator TOUGH2 (Pruess et al., 1999) along with equation-of-state package ECO2N (Pruess and Spycher, 2007). Note that we ignore the effect of fluid compressibility, temperature variations and mutual partitioning between the invading CO_2 and the formation brine.

As discussed above, we have introduced a parameter τ in the MIP model. Incorporation of this parameter allows for invasion only for part of the cells that may be invaded faster than the other possible cells at each percolation step. We have tested different values for τ, and found that a value of $\tau = 0.4$ can produce results that match those from TOUGH2/ECO2N simulations well. Comparison for CO_2

saturations between the MIP model and ECO2N simulation for an example realization is shown in Fig. 1. It can be seen that the MIP model can predict the CO_2 distribution reasonably well. Fig. 2(a, b) shows the simulated capillary pressure curves and their averages. For comparison purposes, we have also plotted the results obtained with $\tau = 1$ (Fig. 2c, d), which provide a less good match with the TOUGH2/ECO2N simulation results. It should be noted that, on average, the MIP model with $\tau = 0.4$ (Fig. 2b) tends to underestimate the brine saturation in the system, when large-scale averaged pressure difference between the CO_2 and the brine is larger than about 30 kPa. This is attributed to the assumption of ignoring the viscous forces in the percolation model. When the pressure drive becomes higher, the viscous pressure loss becomes more comparable to the local capillary pressures.

Breakthrough capillary pressure

It is common and convenient to assume the Leverett scaling relationship (Leverett, 1941) for numerical investigation of two-phase flow in heterogeneous media. Given the same porosity and interfacial tension, the Leverett relationship states that capillary pressure is inversely proportional to square root of permeability. The relationship is supported by laboratory experiments (Dumore and Schols, 1974). It is of interest to see whether the large-scale capillary pressure scales the same way with the upscaled permeability.

Here we study the large-scale breakthrough capillary pressure (P_b) which may be considered as a characteristic capillary pressure for the large scale. Breakthrough capillary pressure in this study is defined as the externally applied pressure at which the non-wetting phase connects through the medium. We have obtained the upscaled absolute permeabilities in the horizontal direction (k_x) through solving the single phase pressure equation.

We have calculated P_b for 400 permeability fields (Case 1~4). As seen in Fig. 3, P_b shows a strong correlation with k_x (correlation coefficient = 0.79). When all 400 data pairs are used for linear regression with the Leverett equation (Fig. 3a), the relative residual is 0.34; whereas if only the case with sand proportion of 0.8 is considered, the relative residual is 0.16 (Fig. 3b). This indicates that the linear relationship may not well describe the data with smaller sand proportions (smaller k_x, larger $(1/k_x)^{0.5}$).

Effect of material proportions

Relative proportions of different materials are one set of the main parameters that control the structure of the Markovian indicator random fields. We here consider a trimodal heterogeneous medium and set the clay material proportion as constant (0.1) while varying the proportions of the sandstone and the siltstone (Case 1-4). Fig. 4 and Fig. 5 show the simulated large-scale capillary pressure and relative permeability curves for the four cases. Visual inspection of the spreading of curves shows a trend of increasing inter-realization variability with decreased proportion of the background material sandstone. This trend is confirmed by, for example, checking the variance of $S_{w,L}$ values for a given capillary pressure. Comparison of the ensemble average curves (Fig. 6) shows that increasing the sandstone proportion leads to a decreased capillary pressure. This is expected since the sandstone material has a smaller local capillary pressure than the two other materials. It can also be seen in Fig. 5 that, for all four proportions, the ensemble average large-scale relative permeability of brine is smaller than that at the local-scale, whereas the ensemble average CO_2 relative permeability is larger than the local-scale values. This may be due to the trapping of brine in the system. Trapped regions of brine have high local brine saturation and high local relative permeability but are connected to the brine flow paths at large scale. Therefore, the trapped brine can shift the large-scale averaged brine saturation to a greater value for the same relative

permeabilities as at the local scale. It is also interesting to note that the large-scale relative permeability curves for the gas (CO_2) phase are spread above and below the local curves, unlike the large-scale relative permeability curves of the liquid phase which tend to fall below the local curves. This is because the gas phase prefers to reside in high permeability regions and the effect of brine-trapping regions on the CO_2 flow paths will be much less pronounced than on the liquid flow. Increasing the sandstone proportion also results in an increase in brine relative permeability and, at the same time, a decrease in CO_2 relative permeability. As a result, the cross point for the brine and CO_2 relative permeability curves is shifted to a smaller $S_{w,L}$ when the sandstone proportion is increased. In other words, the brine and CO_2 relative permeability curves move toward the local curves as the sand proportion increases. However, it should be noted that the influence of material proportion on relative permeability curves is relatively small, considering the large inter-realization variability for all the cases.

It is also interesting to observe in Fig. 4 that many individual capillary pressure curves show a staircase pattern. This kind of patterns has been discussed for mercury porosimetry (e.g., Thompson et al., 1987) and pore-network models (Berkowitz and Ewing, 1998). These staircase patterns may be explained the effect of finite domain size in respect to the siltstone facies (see, e.g., Sahimi, 2011), since some siltstone cells may exist as critical 'throat' points for the invasion front and invasion into these cells requires a much higher pressure than that in the sandstone cells. For larger sandstone proportions (e.g. 0.8 in Fig. 4d), this finite-size effect almost disappears.

Effect of permeability standard deviation within each material

The effect of permeability standard deviation ($\sigma_{\lg k}$) within the sandstone and the siltstone on the large-scale constitutive relationships is also analyzed. The sandstone

and siltstone proportions are fixed at 0.6 and 0.3, respectively. These values fall into the range of values obtained from the borehole data from the Southwest Scania site. Variability in local permeability in the clay material is not studied, since the clay is a minor material and has a large displacement (entry) pressure which prevents the invasion of the supercritical CO_2. In the design of the parametric sensitivity study of permeability standard deviation, it is assumed that the permeability of the sandstone has a larger variability than that of the siltstone.

Fig. 7 and Fig. 8 show the large-scale capillary pressure and relative permeability curves for the three cases with different $\sigma_{\lg k}$ values for sandstone. It can be seen in Fig. 7d that, on average, a larger $\sigma_{\lg k}$ of the sandstone permeability requires a higher capillary pressure for a given brine saturation. It can also be seen that the spreading of the curves is similar for the three cases (Fig. 7a, b, c). For relative permeabilities, shown in Fig. 8, increasing in $\sigma_{\lg k}$ (of the sandstone) leads to a decrease in both the wetting phase and non-wetting phase mobilities.

The effect of $\sigma_{\lg k}$ of the siltstone material is displayed in Fig. 9 and Fig. 10. It is shown in Fig. 9 that, while $\sigma_{\lg k}$ of the siltstone, on average, affects the capillary pressure curve to a small extent, the inter-realization variability seems to decrease with increasing $\sigma_{\lg k}$ of the siltstone. This can be seen, for example, by looking at the $S_{w,L}$ values for $P_{c,L}$ = 30 kPa. However, the ensemble average relative permeability curve is not affected by the $\sigma_{\lg k}$ of the siltstone. In addition, there is no apparent effect of $\sigma_{\lg k}$ of the siltstone on the inter-realization variability in the relative permeability curves.

It is also interesting to note in Fig. 9a that, for small $\sigma_{\lg k}$ (= 0.1) of the siltstone, the large-scale capillary pressure curves exhibit a clear curvature change in the medium saturation range. While for larger $\sigma_{\lg k}$ values of the siltstone (Fig. 9b, c) this curvature change behavior is not exhibited. The reason is that a smaller standard deviation

means a smaller probability to have large permeability (or small entry pressure) cells in the siltstone facies for the non-wetting fluid to invade. Thus the siltstone may function as a blockage at some critical cells for the invasion pressures corresponding to the medium saturation range when the standard deviation in siltstone permeabilities is small. Also it is expected that this curvature change behavior will not be seen when the sand proportion is high (e.g 0.8).

Effect of correlation length within each material

We have compared results from two cases with different correlation lengths in the sandstone and in the siltstone. The correlation lengths in the second case (Case 10) are one third of those in the first case (Case 2). Results (Fig. 11) show that the large-scale constitutive relationships are not affected by the decrease in correlation lengths. Inter-realization variability is also similar for the two cases. In other words, the variability of the distribution of the facies and their relative lengths (these two are interrelated as can be seen in Table 1) are far more crucial than the correlation length within the facies.

Application of upscaled constitutive relationships

In order to test the performance of the upscaled capillary pressure-saturation relationships and relative permeability relationships when applied to an upscaled homogeneous model for the domain, we have carried out simulations of CO_2 injection and migration. Results for an example realization of the heterogeneous permeability fields of Case 2 (Table 1) are discussed here. The upscaled capillary pressure-saturation relationship can be well fitted to the van Genuchten function (van Genuchten, 1980) $P_{c,L} = \alpha\left[(S_{e,L})^{-1/m} - 1\right]^{1/n}$ where $S_{e,L}$ is the large-scale effective brine saturation. $S_{e,L}$ is defined as $S_{e,L} = (S_{w,L} - S_{wr,L})/(1 - S_{wr,L})$ where $S_{w,L}$ is large-scale brine saturation and $S_{wr,L}$ is large-scale residual brine saturation. The fitting

parameters are α = 7680 Pa, m = 0.509, n = 2.04 and $S_{wr,L}$ = 0.302, respectively. The upscaled liquid phase relative permeability relationship can be well fitted to the Brooks-Corey model given in Krevor et al. (2012) as $k_{rw,L} = S_{e,L}^{Nw}$ where the fitting parameter N_w = 8.5. The upscaled gas phase relative permeability can be fitted to obtain a functional form of $k_{rn,L} = 0.7(1-S_{e,L})^3$. Figures showing the fitting of the constitutive relationships are not presented here for space considerations. The upscaled absolute permeability of 2.2×10^{-13} m^2 is used for the homogeneous model. CO_2 injection with a rate of 0.18×10^{-2} kg/s is simulated for both the heterogeneous domain and the homogeneous domain. Fig. 12 presents the comparison between the heterogeneous and the upscaled homogeneous model for the CO_2 saturation profile (the saturation is averaged in the direction normal to injection). It can be seen that the upscaled homogeneous model can provide reasonable results in terms of CO_2 migration through the domain, suggesting that the upscaling method works properly for this strongly heterogeneous system.

Discussions and conclusions

The macroscopic percolation theory has been employed to investigate the large-scale constitutive relationships for multimodal heterogeneous media. A macroscopic invasion percolation (MIP) model has been developed, based on the assumption of dominance of capillary forces. Comparison of the MIP model with the numerical simulator TOUGH2/ECO2N for simulations of large-scale drainage capillary pressure curves shows a good agreement when the large-scale pressure drive in the system is below about 30000 Pa. When higher driving pressure is encountered, the MIP model tends to underestimate the brine saturation to some extent. This is due to the assumption of ignoring the viscous forces, since the viscous pressure loss become more comparable to the local capillary pressures as the pressure difference

increases. However, given the simplicity of the MIP model, the small error introduced can be considered well justified, since Monte Carlo simulations for two-phase flow in heterogeneous media with large grids by using numerical models such as TOUGH2/ECO2N will be highly impractical due to the expensive computational cost.

Large-scale constitutive relationships have been constructed through simulation procedures of CO_2 displacing brine in multimodal heterogeneous media for ten different cases of heterogeneity, described through their geostatistical parameters. Data from a saline aquifer at the Southwest Scania site, Sweden is used as a basis when generating the data sets. To generate the multimodal heterogeneous permeability fields, we have combined transition-probability based indicator random fields with Gaussian random fields, following the method of Lu and Zhang (2002).

We have studied the relationship between the large-scale breakthrough capillary pressure (P_b) and the upscaled absolute permeability in the horizontal direction (k_x). P_b can be considered as a characteristic macro-scale capillary pressure. Results indicate that the Leverett equation may well describe the P_b -k_x relationship when the sandstone (background material) proportion is high (>0.7), i.e., the system is relatively homogeneous. For macro-scale systems with smaller sandstone proportions it may not be appropriate to link capillary pressure and absolute permeability through the Leverett equation.

Material proportions affect the large-scale constitutive relationships. It is shown that, on average, increasing the sandstone proportion leads to decreased capillary pressure, slightly increased brine relative permeability and slightly decreased CO_2 relative permeability. The constitutive relationships are also influenced by the permeability standard deviation ($\sigma_{\lg k}$) both within the sandstone material and within the siltstone material. The ensemble average relative permeabilities (Fig. 8) for both phases are higher when $\sigma_{\lg k}$ in the sandstone is smaller. The ensemble average

constitutive relationships are not significantly affected by σ_{lgk} in the siltstone (Fig. 9 and Fig. 10), but, interestingly, the inter-realization variability of capillary pressure permeabilities seems to increase with decreasing σ_{lgk} in the siltstone. The constitutive relationships are not influenced by the correlation lengths within each material.

To sum up, the large-scale constitutive relationships are mainly controlled by the proportion and the permeability variability of the sandstone material, while the existence of the other materials and their permeability variability may contribute, in a complex way, to the uncertainty in the large-scale constitutive relationships.

It should be noted that we have assumed the top and bottom boundary to impermeable. Thus, upscaled flow is forced to be essentially one-dimensional. This assumption may be suitable for field situations where the lateral dimension is much larger than the vertical and the dominant CO_2 migration direction is in the lateral. However, for situations where the flow in both directions is important for the prediction on the spatial scale of interest, two-dimensional upscaling may be needed. For further study along this line, the presented methodology herein may be extended to have periodic instead of impermeable boundary conditions.

Finally, it should be pointed out that we have focused on the primary drainage process which describes CO_2 migration during the injection period. However, for the post-injection period, imbibition of the wetting phase (brine) needs to be considered. Modeling of the large-scale imbibition process first requires the descriptions of the local-scale imbibition capillary pressure curves. Then large-scale imbibition may be macroscopically modeled as an ordinary percolation process (Ewing and Gupta, 1993; Ioannidis et al., 1996). For CO_2 storage problems, an important topic is residual trapping of the non-wetting fluid (CO_2). It is therefore of interest to evaluate the effect of multimodal heterogeneous formation on the large-scale residual trapping

which may be quite different from the local trapping behavior. This motivates further investigations.

Acknowledgment.

Funding for this work was provided by the European Community's Seventh Framework Programme (FP7/MUSTANG project) and the Swedish Research Council (Vetenskapsrådet). We thank two anonymous reviewers for constructive comments which helped improving the manuscript.

References

Ambrose, W. A., S. Lakshminarasimhan, M. H. Holtz, V. Núñez-López, S. D. Hovorka, and I. Duncan (2008), Geologic factors controlling CO2 storage capacity and permanence: case studies based on experience with heterogeneity in oil and gas reservoirs applied to CO2 storage, *Environmental Geology*, *54*(8), 1619-1633, doi:10.1007/s00254-007-0940-2.

Bellin A., Y. Rubin (1996), Hydro_gen: A spatially distributed random field generator for correlated properties, Stochastic Hydrology and Hydraulics, 10(4), 253-278.

Berkowitz, B., and R. P. Ewing (1998), Percolation theory and network modeling, *Surveys in Geophysics*, 19, 23–72.

Bolster, D., M. Dentz, and J. Carrera (2009), Effective two-phase flow in heterogeneous media under temporal pressure fluctuations, *Water Resour. Res.*, *45*(5), W05408, doi:10.1029/2008WR007460.

Bolster, D., I. Neuweiler, M. Dentz, and J. Carrera (2011), The impact of buoyancy on front spreading in heterogeneous porous media in two-phase immiscible flow, *Water Resour. Res.*, *47*(2), W02508, doi:10.1029/2010WR009399.

Braun, C., R. Helmig, and S. Manthey (2005), Macro-scale effective constitutive relationships for two-phase flow processes in heterogeneous porous media with

emphasis on the relative permeability–saturation relationship, *Journal of Contaminant Hydrology*, *76*(1–2), 47-85, doi:10.1016/j.jconhyd.2004.07.009.

Brooks R. H., and A. T. Corey (1964), Hydraulic properties of porous media. Hydrology paper 3, Colorado State University, Fort Collins, Colorado.

Carle, S. F., and G. E. Fogg (1996), Transition probability-based indicator geostatistics, *Math. Geol.*, 28(4), 453–476.

Carle, S. F., and G. E. Fogg (1997), Modeling spatial variability with one- and multi-dimensional continuous Markov chains, *Math. Geol.*, 29(7), 891–918.

Desbarats, A. J. (1990), Macrodispersion in sand-shale sequences, *Water Resour. Res.*, *26*(1), 153-163, doi:10.1029/WR026i001p00153.

Doughty, C. (2007), Modeling geologic storage of carbon dioxide: Comparison of non-hysteretic and hysteretic characteristic curves, *Energy Conversion and Management*, *48*(6), 1768-1781, doi:10.1016/j.enconman.2007.01.022.

Doughty, C., and K. Pruess (2004), Modeling supercritical carbon dioxide injection in heterogeneous porous media, *Vadose Zone J*, *3*(3), 837-847, doi:10.2113/3.3.837.

Dumore, J. M., and R. S. Schols (1974), Drainage capillary pressure functions and the influence of connate water, SPE J., 14, 437-444.

Eichel, H., R. Helmig, I. Neuweiler, and O. A. Cirpka (2005), Upscaling of two-phase flow processes in porous media. In: Das, D.B. & S.M. Hassanizadeh (eds.): Upscaling Multiphase Flow in Porous Media. Springer-Verlag, 237-257.

Ewing, R. P., and S. C. Gupta (1993), Modeling percolation properties of random media using a domain network, *Water Resour. Res.*, *29*(9), 3169-3178, doi:10.1029/93WR01496.

Flett, M.A., R.M. Gurton and I.J. Taggart (2005), Heterogeneous saline formations: Long-term benefits for geo-sequestration of greenhouse gases. Proceedings of

the 7th International Conference on Greenhouse Gas Control Technologies (GHGT-7), September 5–9, 2004, Vancouver, Canada, v.I, 501-510

Flett, M., R. Gurton, and G. Weir (2007), Heterogeneous saline formations for carbon dioxide disposal: Impact of varying heterogeneity on containment and trapping, *Journal of Petroleum Science and Engineering*, *57*(1-2), 106-118, doi:10.1016/j.petrol.2006.08.016.

Gasda, S. E., and M. a. Celia (2005), Upscaling relative permeabilities in a structured porous medium, *Advances in Water Resources*, *28*(5), 493-506, doi:10.1016/j.advwatres.2004.11.009.

Gunnarsson, N. (2011), 3D modeling in Petrel of geological CO_2 storage site, Master thesis, 62 pp., Uppsala University, Uppsala.

Han, W. S., S.-Y. Lee, C. Lu, and B. J. McPherson (2010), Effects of permeability on CO2 trapping mechanisms and buoyancy-driven CO2 migration in saline formations, *Water Resour. Res.*, *46*(7), W07510, doi:10.1029/2009WR007850.

Ioannidis, M. A., I. Chatzis, and F. A. L. Dullien (1996), Macroscopic percolation model of immiscible displacement: effects of buoyancy and spatial Structure, *Water Resour. Res.*, *32*(11), 3297-3310, doi:10.1029/95WR02216.

IPCC (2005), IPCC special report on carbon dioxide capture and storage. In: Metz, B., Davidson, O., de Coninck, H.C., Loos, M., Meyer, L.A. (editors.), Prepared by Working Group III of the Intergovernmental Panel on Climate Change, Cambridge University Press, Cambridge and New York, NY, 442 pp.

Juanes, R., E. J. Spiteri, F. M. Orr Jr., and M. J. Blunt (2006), Impact of relative permeability hysteresis on geological CO2 storage, *Water Resour. Res.*, *42*(12), W12418, doi:10.1029/2005WR004806.

Keilegavlen, E., J. M. Nordbotten, and A. F. Stephansen (2012), Tensor relative permeabilities: origins, modeling and numerical discretization, *International Journal of Numerical Analysis and Modeling*, *9*(3), 701-724.

Kitajima, H., T. Shimamoto, and W. Tanikawa (2005), Estimation of porosity and permeability structures of Miyazaki Group, Japan, *Eos Trans. AGU, 86*(52), Fall Meet. Suppl., Abstract #T53C-1445.

Krevor, S. C. M., R. Pini, L. Zuo, and S. M. Benson (2012), Relative permeability and trapping of CO2 and water in sandstone rocks at reservoir conditions, *Water Resour. Res.*, *48*(2), W02532, doi:10.1029/2011WR010859.

Kueper, B. H., and D. B. McWhorter (1992), The use of macroscopic percolation theory to construct large-scale capillary pressure curves, *Water Resour. Res.*, *28*(9), 2425-2436, doi:10.1029/92wr01176.

Lengler, U., M. De Lucia, and M. Kühn (2010), The impact of heterogeneity on the distribution of CO2: Numerical simulation of CO2 storage at Ketzin, *International Journal of Greenhouse Gas Control*, *4*(6), 1016-1025, doi:10.1016/j.ijggc.2010.07.004.

Lenormand, R., E. Touboul, and C. Zarcone (1988), Numerical models and experiments on immiscible displacements in porous media, *Journal of Fluid Mechanics*, *189*, 165–187.

Leverett, M. C. (1941), Capillary behavior in porous solids, Trans. Am. Inst. Min. Metall. Pet. Eng., 142,341-358.

Lewandowska, J., A. Szymkiewicz, K. Burzyński, and M. Vauclin (2004), Modeling of unsaturated water flow in double-porosity soils by the homogenization approach, *Advances in Water Resources*, *27*(3), 283-296.

Lu, Z., and D. Zhang (2002), On stochastic modeling of flow in multimodal heterogeneous formations, *Water Resour. Res.*, *38*(10), 1190, doi:10.1029/2001WR001026.

Mantoglou, A., and L. W. Gelhar (1987), Stochastic modeling of large-scale transient unsaturated flow systems, *Water Resour. Res.*, *23*(1), 37-46, doi:10.1029/WR023i001p00037.

Mouche, E., M. Hayek, and C. Mügler (2010), Upscaling of CO2 vertical migration through a periodic layered porous medium: The capillary-free and capillary-dominant cases, *Advances in Water Resources*, *33*(9), 1164-1175, doi:10.1016/j.advwatres.2010.07.005.

Neuweiler, I., and H.-J. Vogel (2007), Upscaling for unsaturated flow for non-Gaussian heterogeneous porous media, *Water Resour. Res.*, *43*(3), W03443, doi:10.1029/2005WR004771.

Obi, E.-O. J., and M. J. Blunt (2006), Streamline-based simulation of carbon dioxide storage in a North Sea aquifer, *Water Resour. Res*., 42, W03414, doi:10.1029/2004WR003347.

Pini, R., S. C. M. Krevor, and S. M. Benson (2012), Capillary pressure and heterogeneity for the CO2/water system in sandstone rocks at reservoir conditions, *Advances in Water Resources*, *38*, 48-59.

Pruess, K., and J. Garcia (2002), Multiphase flow dynamics during CO2 disposal into saline aquifers, *Environ. Geol., 42*(2–3), 282–295.

Pruess, K., C. Oldenburg, and G. Moridis (1999), TOUGH2 User's Guide, Version 2.0, Report LBNL-43134, Lawrence Berkeley National Laboratory, Berkeley, California.

Pruess, K., and N. Spycher (2007), ECO2N – A fluid property module for the TOUGH2 code for studies of CO2 storage in saline aquifers, *Energy Conversion and Management*, *48*(6), 1761-1767, doi:10.1016/j.enconman.2007.01.016.

Quintard, M., and S. Whitaker (1990), Two-phase flow in heterogeneous porous media I: The influence of large spatial and temporal gradients, *Transport in Porous Media*, *5*(4), 341-379, doi:10.1007/BF01141991.

Ringrose, P. S., A. W. Martinius, and J. Alvestad (2008), Multiscale geological reservoir modelling in practice , *Geological Society, London, Special Publications* , *309* (1), 123-134.

Rubin, Y. (1995), Flow and transport in bimodal heterogeneous formations, *Water Resour. Res.*, *31*(10), 2461-2468, doi:10.1029/95WR01953.

Russo, D., J. Zaidel, and A. Laufer (2001), Numerical analysis of flow and transport in variably saturated bimodal heterogeneous porous media, *Water Resour. Res.*, *37*(8), 2127-2141, doi:10.1029/2001WR000393.

Saadatpoor, E., S. Bryant, and K. Sepehrnoori (2010), New trapping mechanism in carbon sequestration, *Transport in Porous Media*, *82*(1), 3-17, doi:10.1007/s11242-009-9446-6.

Sahimi, M. (2011), *Flow and transport in porous media and fractured rock*, 718 pp., Wiley-VCH Verlag, Weinheim, Germany, p. 598-599.

Shamshiri, H., and B. Jafarpour (2012), Controlled CO2 injection into heterogeneous geologic formations for improved solubility and residual trapping, *Water Resour. Res.*, *48*(2), W02530, doi:10.1029/2011WR010455.

Silva, O., I. Neuweiler, M. Dentz, M. Saaltink and J. Carrera (2012), Upscaling of two-phase flow processes in CO2 geological storage, Geophysical Research Abstracts, Vol. 14, EGU2012-6056, EGU General Assembly, 2012.

Thompson, A. H., A. J. Katz, and R. A. Raschke (1987), Mercury injection in porous media: A resistance devil's staircase with percolation geometry, *Physical Review Letters*, *58*(1), 29–32, doi:10.1103/PhysRevLett.58.29.

Tidwell, V. C., and J. L. Wilson, Heterogeneity, permeability patterns, and permeability upscaling: Physical characterization of a block of Massillon Sandstone exhibiting nested scales of heterogeneity, SPE Reservoir Eval. Eng., 3(4), 283–291, 2000.

Tsang, C.-F., J. Birkholzer, and J. Rutqvist (2007), A comparative review of hydrologic issues involved in geologic storage of CO2 and injection disposal of liquid waste, *Environmental Geology*, *54*(8), 1723-1737, doi:10.1007/s00254-007-0949-6.

Van Genuchten, M. T. (1980), A closed-form equation for predicting the hydraulic conductivity of unsaturated soils, *Soil Sci. Soc. Am. J.*, 44, 892-898.

Wilkinson, D., and J. F. Willemsen (1983), Invasion percolation: A new form of percolation theory, *J. Phys. A Math. Gen*., 16, 3365– 3376.

Wolff, M., B. Flemisch, R. Helmig, and I. Aavatsmark (2012), Treatment of tensorial relative permeabilities with multipoint flux approximation, *International Journal of Numerical Analysis and Modeling*, *9*(3), 725-744.

Yeh, T.-C. J., L. W. Gelhar, and A. L. Gutjahr (1985a), Stochastic analysis of unsaturated flow in heterogeneous soils: 1. Statistically isotropic media, *Water Resour. Res.*, *21*(4), 447-456, doi:10.1029/WR021i004p00447.

Yeh, T.-C. J., L. W. Gelhar, and A. L. Gutjahr (1985b), Stochastic analysis of unsaturated flow in heterogeneous soils: 2. Statistically anisotropic media with variable α, *Water Resour. Res.*, *21*(4), 457-464, doi:10.1029/WR021i004p00457.

Yortsos, Y. C., C. Satik, J.-C. Bacri, and D. Salin (1993), Large-scale percolation theory of drainage, Transport in Porous Media, 10(2), 171-195, doi:10.1007/BF00617007.

Zhang, D. (1999), Nonstationary stochastic analysis of transient unsaturated flow in randomly heterogeneous media, *Water Resour. Res.*, *35*(4), 1127-1141, doi:10.1029/1998WR900126.

Table 1. Statistical parameters for the multimodal heterogeneous medium. Subscript 1 stands for sandstone material, 2 for siltstone and 3 for clay.

Case	Material proportions			Mean lens lengths*			Std. Dev. ($\log_{10}$ k)			Correlation lengths*		
	p_1 sand	p_2 silt	p_3 clay	L_1 [m]	L_2 [m]	L_3 [m]	σ_1	σ_2	σ_3	λ_1 [m]	λ_2 [m]	λ_3 [m]
1	0.5	0.4	0.1	1.2	1.0	0.5	0.5	0.4	0.1	0.40	0.33	0.17
2	0.6	0.3	0.1	1.8	1.0	0.5	0.5	0.4	0.1	0.60	0.33	0.17
3	0.7	0.2	0.1	2.5	1.0	0.5	0.5	0.4	0.1	0.83	0.33	0.17
4	0.8	0.1	0.1	3.8	1.0	0.5	0.5	0.4	0.1	1.27	0.33	0.17
5	0.6	0.3	0.1	1.2	1.0	0.5	0.1	0.1	0.1	0.57	0.33	0.17
6	0.6	0.3	0.1	1.2	1.0	0.5	0.5	0.1	0.1	0.57	0.33	0.17
7	0.6	0.3	0.1	1.2	1.0	0.5	1.0	0.1	0.1	0.57	0.33	0.17
8	0.6	0.3	0.1	1.2	1.0	0.5	1.0	0.4	0.1	0.57	0.33	0.17
9	0.6	0.3	0.1	1.2	1.0	0.5	1.0	0.8	0.1	0.57	0.33	0.17
10	0.6	0.3	0.1	1.2	1.0	0.5	0.5	0.4	0.1	0.20	0.11	0.17

*Mean lens lengths and correlation lengths within each material are given in the vertical direction; a factor of 10 is assumed for the quantities in the horizontal direction.

For all cases, categorical geometrical mean permeabilities within each of the three materials are given in Table 2.

Table 2. list of local-scale parameters.

Parameter	Sandstone	Siltstone	Clay	Unit
k	2.76×10^{-13}	1.0×10^{-14}	1.0×10^{-17}	m^2
P_{cd}	3192	16770	530290	Pa
ϕ	0.2	0.2	0.2	
γ	1.4	1.0	0.7	
S_{wr}	0.19	0.2	0.3	

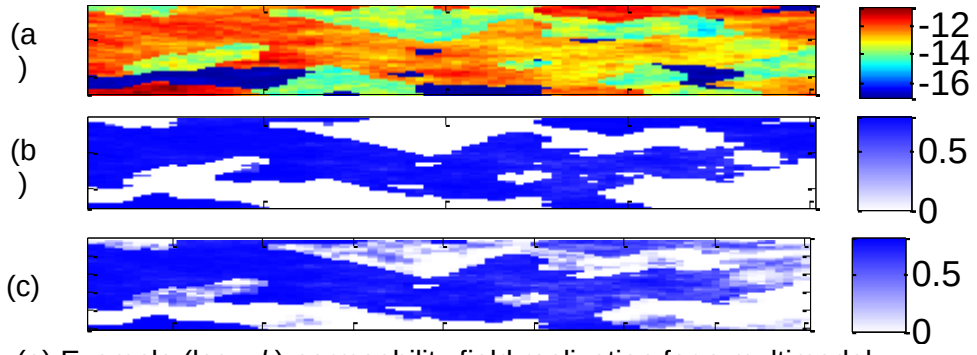

Fig. 1. (a) Example ($\log_{10} k$) permeability field realization for a multimodal heterogeneous medium. (b) CO_2 saturation distribution obtained from the percolation model for an externally applied pressure difference of 20000 Pa between the invading CO_2 and the formation brine. (c) CO_2 saturation distribution obtained from TOUGH2/ECO2N simulation.

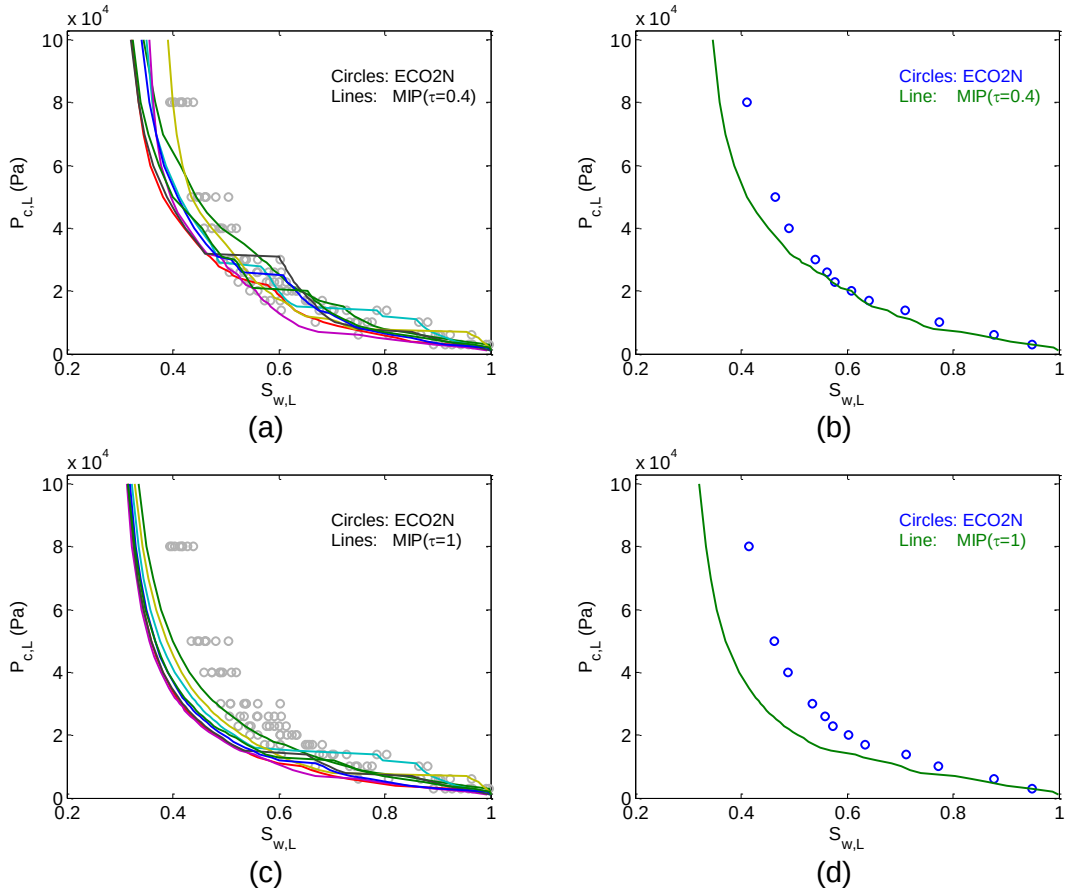

Fig. 2. Comparison of capillary pressure relationships obtained from the macroscopic invasion percolation (MIP) model (lines) and from the numerical simulator TOUGH2/ECO2N (circles). Figure parts: (a), example curves simulated by MIP with parameter τ = 0.4; (b), averaged relationships from the results in (a); (c), example curves simulated by MIP with parameter τ = 1.0; (d), averaged relationships from the results in (c).

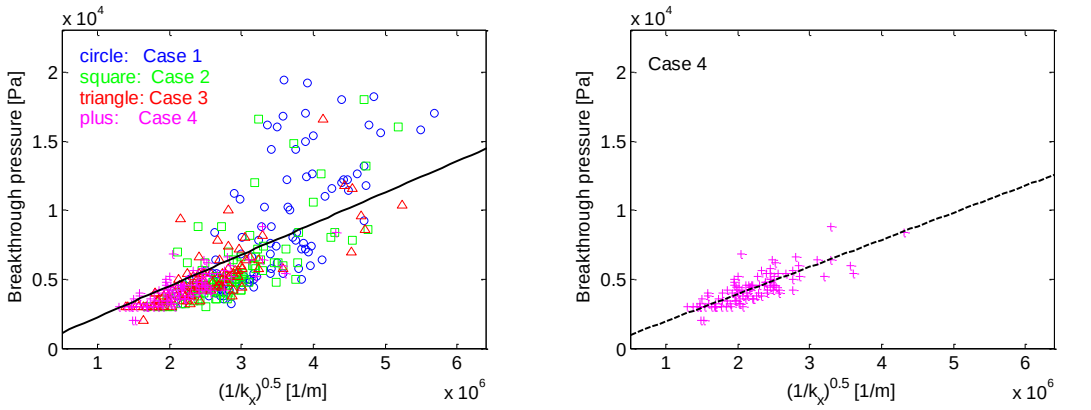

Fig. 3. Breakthrough capillary pressure plotted against large-scale average absolute permeability in the displacement (horizontal) direction. Symbols denote the simulations; lines denote the best fits by the Leverett equation.

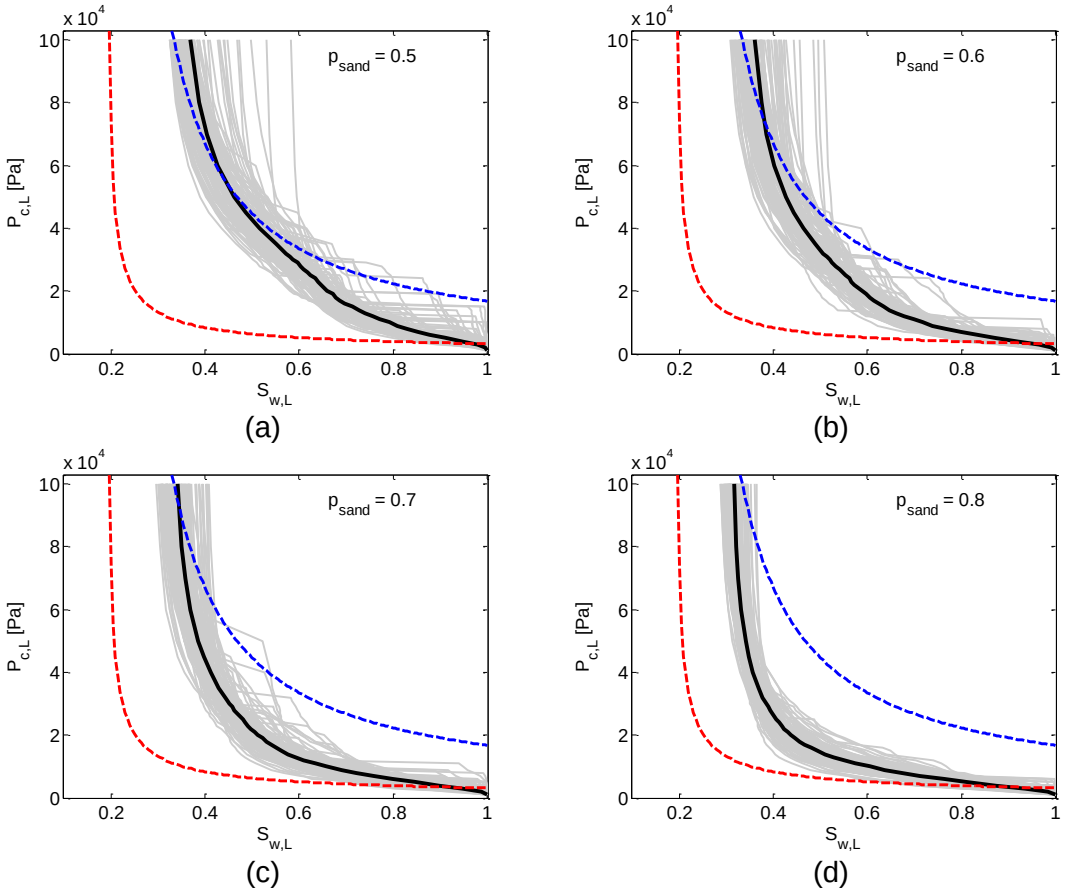

Fig. 4. Effect of sandstone proportion on large-scale capillary pressure curves. Gray lines show results of 100 realizations for each of the four cases. Black lines show the respective averages. The local curves for the sandstone (red dashed lines) and the siltstone (blue dashed lines) are also plotted, with parameters listed in Table 2.

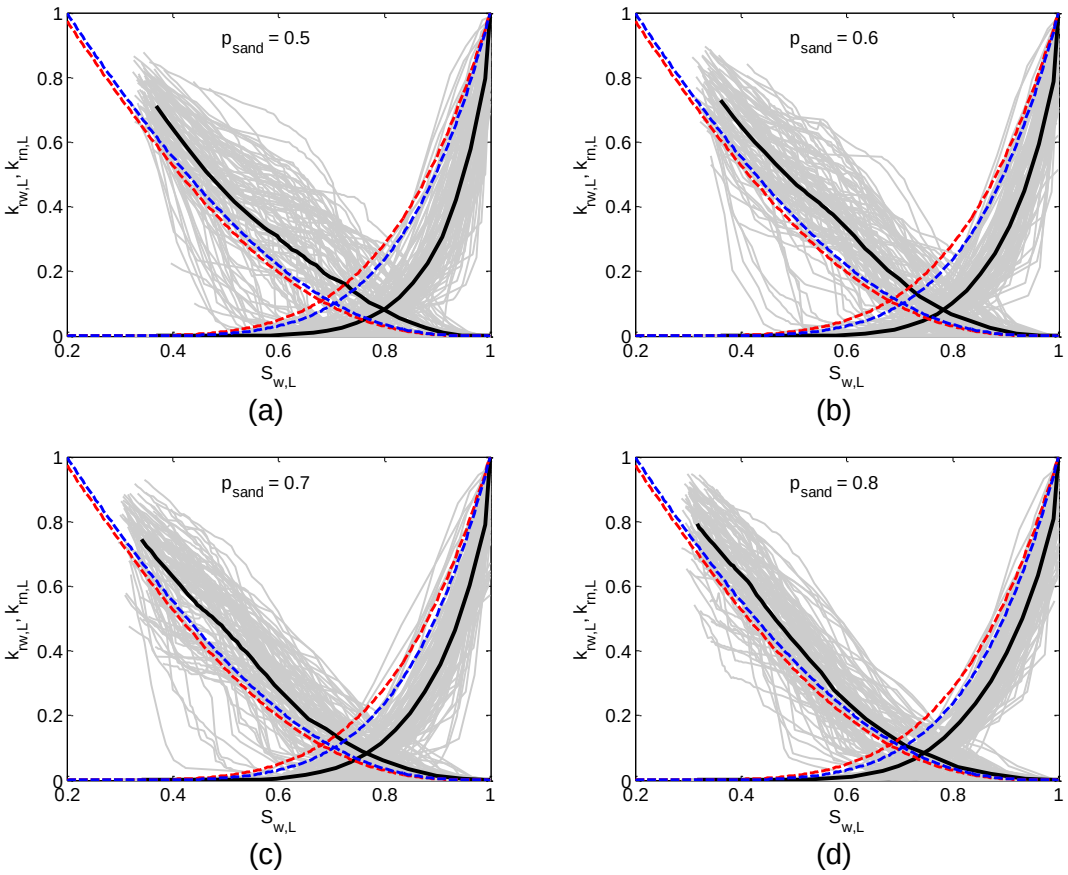

Fig. 5. Effect of sandstone proportion on large-scale relative permeability curves. Gray lines show results of 100 realizations for each of the four cases. Black lines show the respective averages. Red and blue dashed lines show the local relative permeabilities of the sandstone and siltstone, plotted using equations (8) and (9) with parameters listed in Table 2.

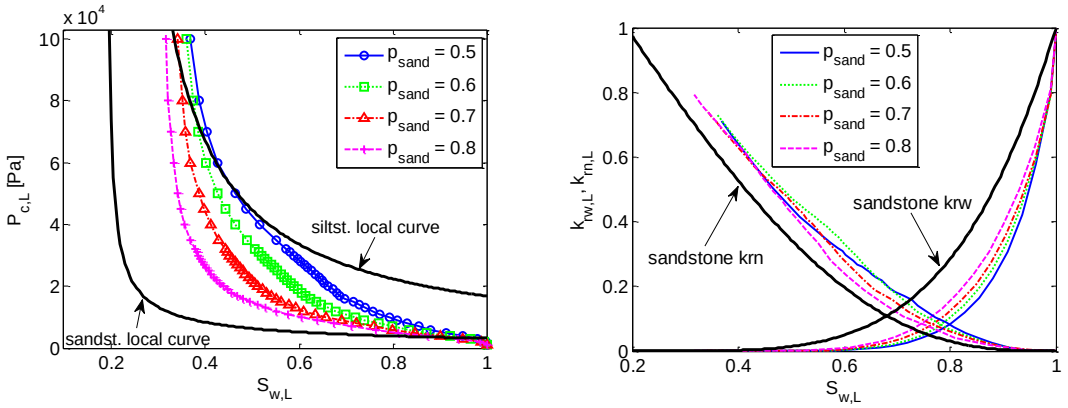

(a) (b)

Fig. 6. Comparison of ensemble average capillary pressure and relative permeability curves for different material proportions.

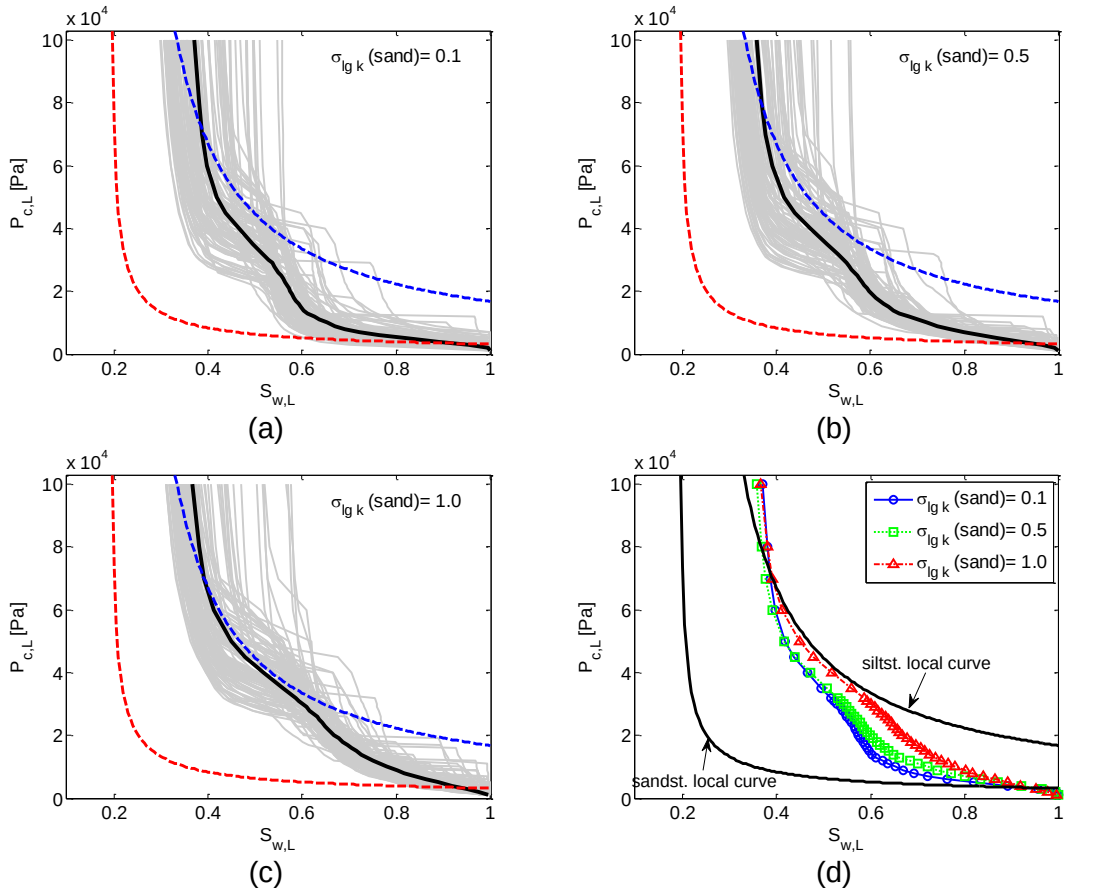

Fig. 7. Effect of permeability ($\log_{10} k$) standard deviation within the sandstone material on large-scale capillary pressure curves. (a, b, c) Gray lines show results of 100 realizations for each of the three cases (Case 5, 6, and 7); black lines show the respective averages; the local curves for the sandstone (red dashed lines) and the siltstone (blue dashed lines) are also plotted. (d) Comparison of the ensemble averages.

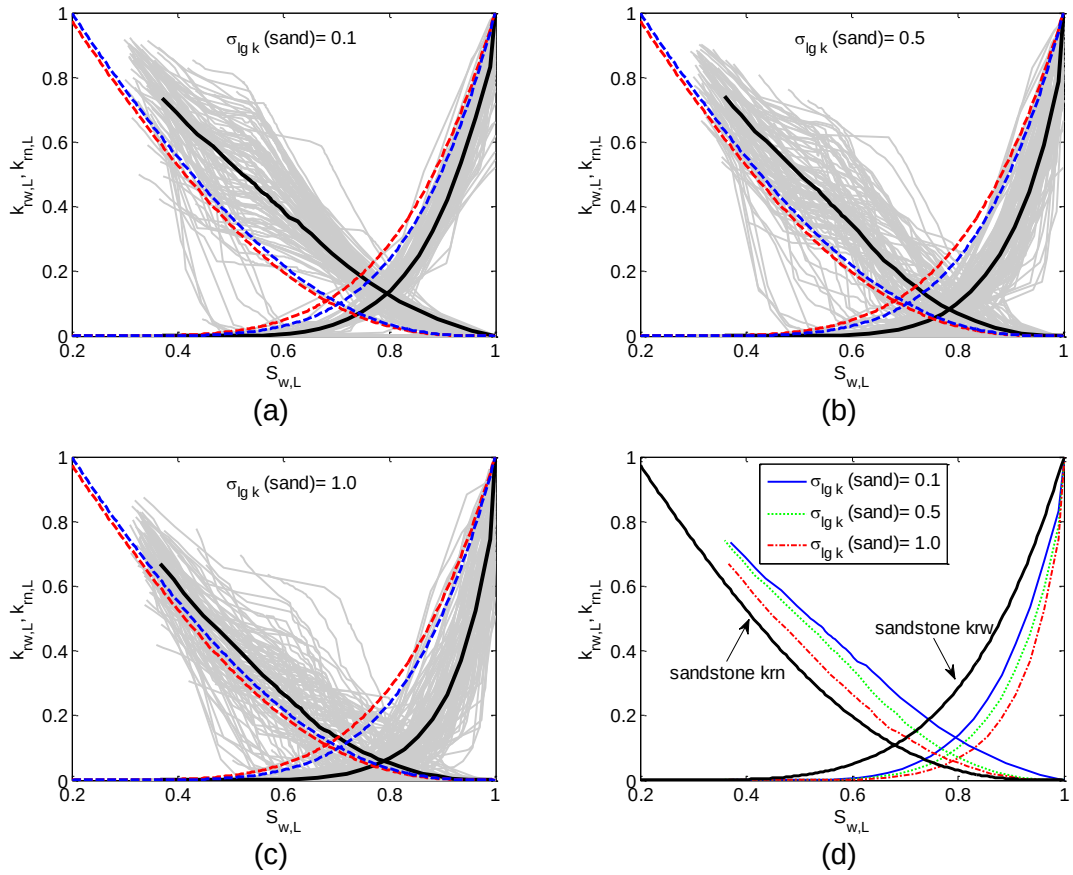

Fig. 8. Effect of permeability ($\log_{10} k$) standard deviation within the sandstone material on large-scale relative permeability curves. (a, b, c) Gray lines show results of 100 realizations for each of the three cases (Case 5, 6, and 7); black lines show the respective averages; red and blue dashed lines show the local relative permeabilities of the sandstone and the siltstone. (d) Comparison of the ensemble averages.

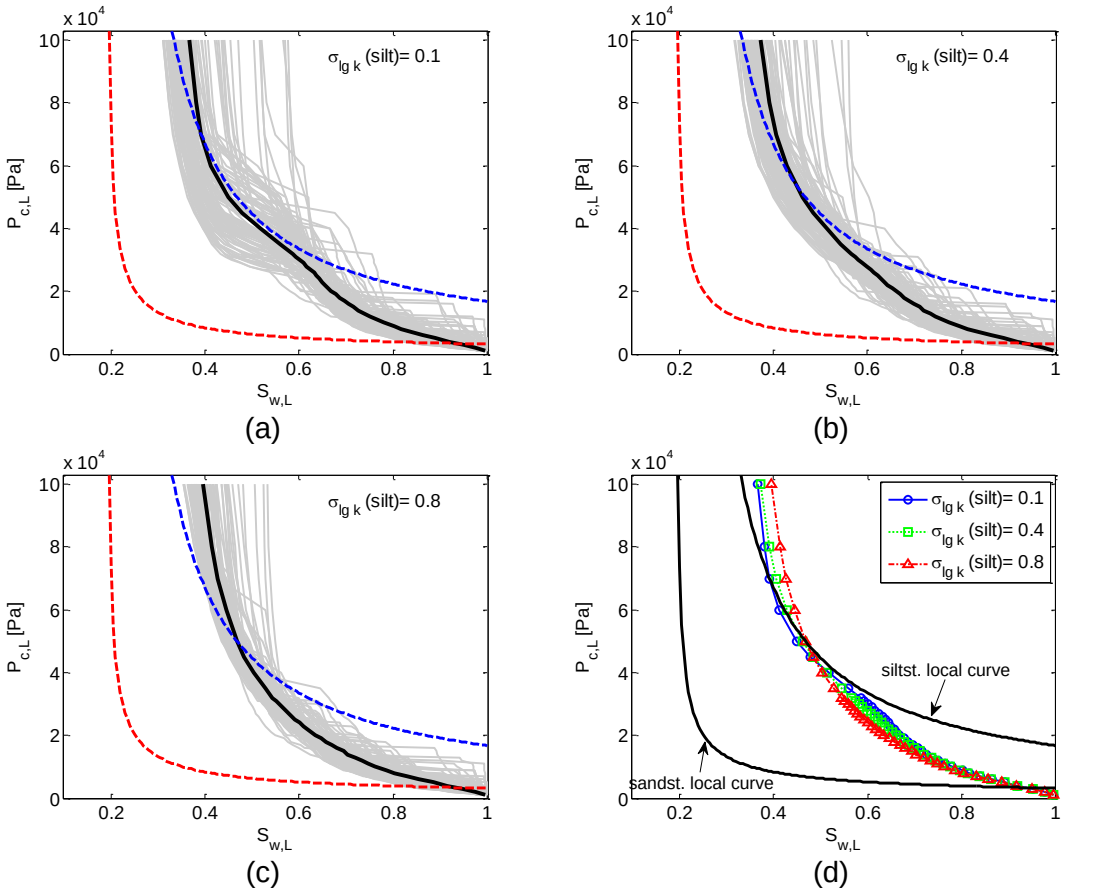

Fig. 9. Effect of permeability ($\log_{10} k$) standard deviation within the siltstone material on large-scale capillary pressure curves. (a, b, c) Gray lines show results of 100 realizations for each of the three cases (Case 7, 8, and 9); thick black lines show the respective averages; the local curves for the sandstone and the siltstone are shown in red and blue dashed lines, respectively. (d) Comparison of the ensemble averages.

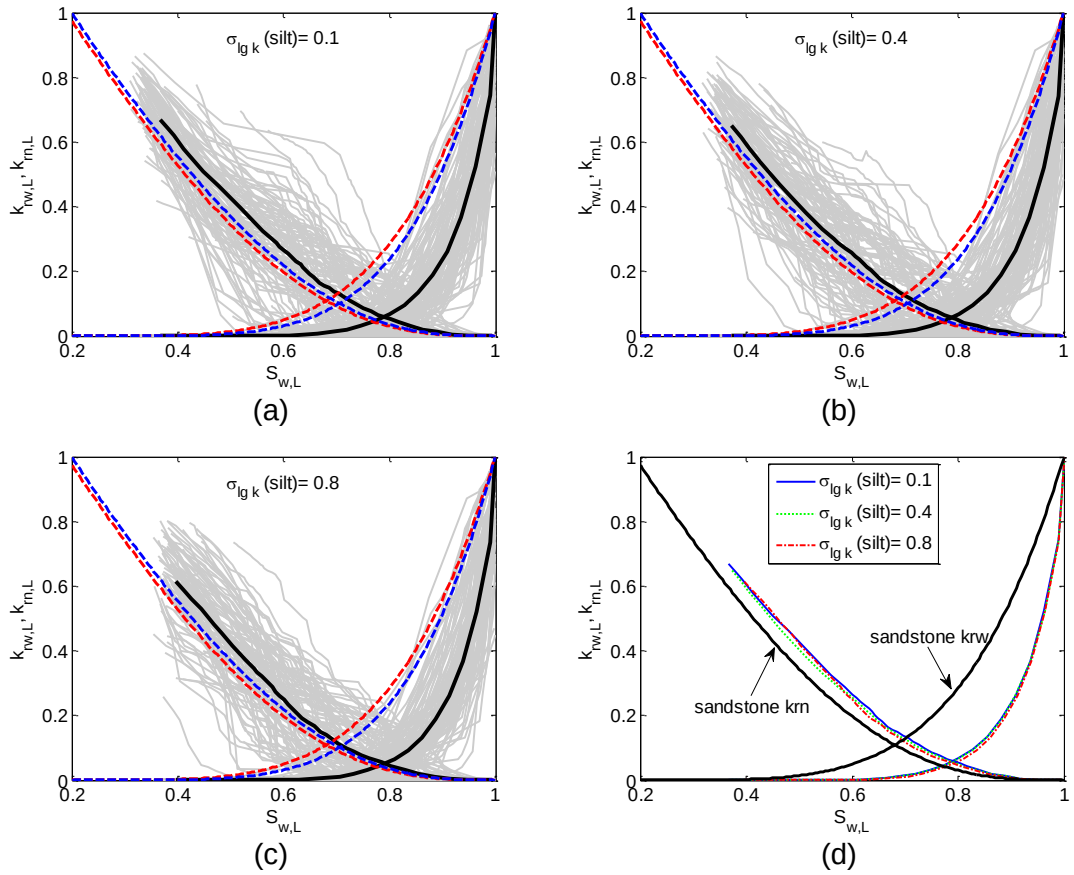

Fig. 10. Effect of permeability ($\log_{10} k$) standard deviation within the siltstone material on large-scale relative permeability curves. (a, b, c) Gray lines show results of 100 realizations for each of the three cases (Case 7, 8, and 9); thick black lines show the respective averages; red and blue dashed lines show the local relative permeabilities of the sandstone and the siltstone. (d) Comparison of the ensemble averages.

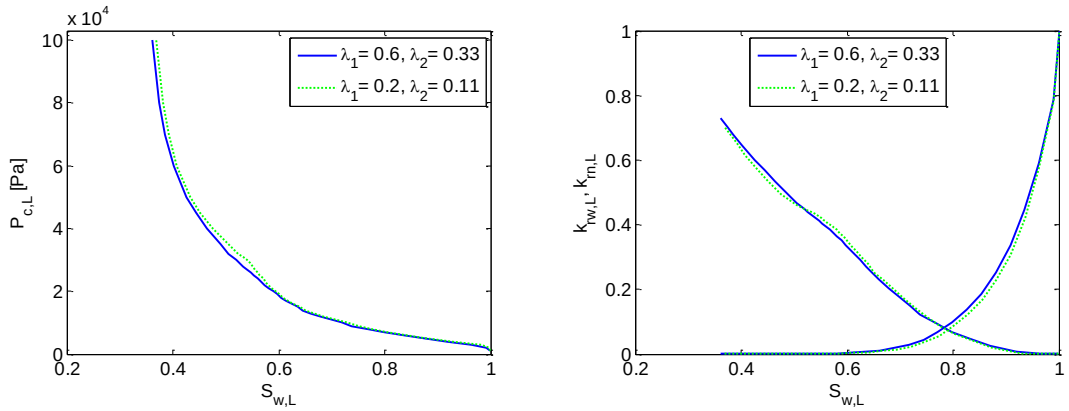

Fig. 11. Comparison of ensemble average capillary pressure and relative permeability curves for different correlation lengths in the sandstone and siltstone (Case 2 and 10).

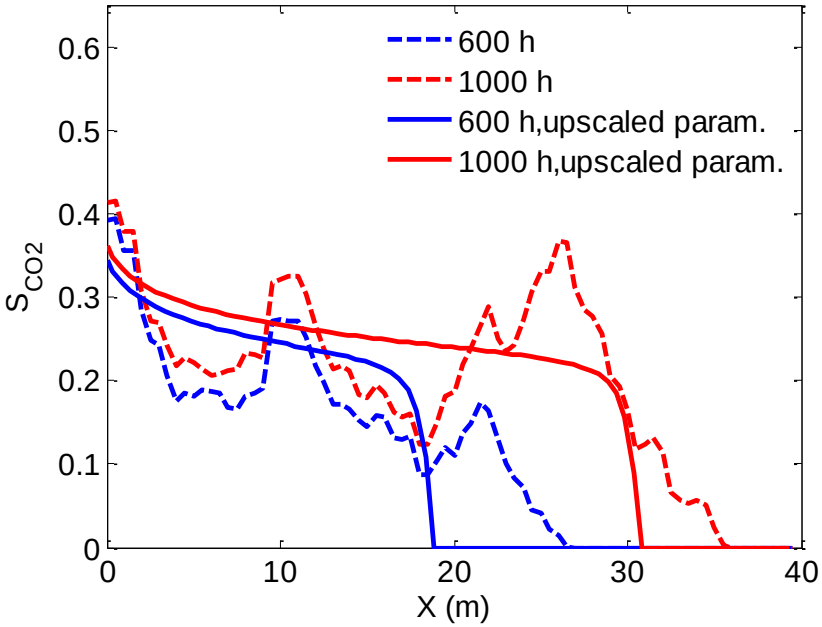

Fig. 12. Comparison of CO2 saturation profile at two different times in the heterogeneous model and the homogeneous model with upscaled parameters.